Nanoscale

ROYAL SOCIETY OF CHEMISTRY

PAPER

View Article Online
View Journal | View Issue

Cite this: *Nanoscale*, 2025, **17**, 1342

Construction of a circularly polarized luminescence sensor based on self-assembly of carbon dots and G-quartet chiral nanofibers†

Dong Wang,[a] Zhiwei Zhang,[a] Xuetao Yan,[a] Tianliang Li,[a] Yingying Chen,[a] Zhenzhen Li*[a] and Lingyan Feng*[a,b]

Circularly polarized luminescence (CPL) is a fascinating luminescence phenomenon that has garnered significant research attention for chiroptical applications. In this study, we developed a highly sensitive chiroptical sensor by co-assembling G-quartet nanofibers and nonchiral nitrogen sulfur-doped carbon dots (N–S-CDs) for dual ion detection. The N–S-CDs were synthesized using the one-step microwave method, and a helical G-quartet-based nanofiber structure (g-fiber) was simultaneously formed from guanosine 5′-monophosphate (GMP) in the presence of Sr^{2+}. An adjustable helical G-quartet-based nanofiber provided an optimal chiral environment for CPL emission, with a dissymmetry factor (g_{lum}) reaching ±0.02. Notably, the left-handed (L-) and right-handed (R-) helical chirality of the complex was determined by switching between kinetic trap states and thermodynamic equilibrium during the reaction process. An optimized CPL sensor was developed based on chiral CDs/g-fiber composite materials, utilizing sensitive CPL as the signal output of dual detection for Hg^{2+} and I^-. Similar limits of detection (LODs) were achieved for both L-/R-nanocomposites, with the best results being 83.5 nM for Hg^{2+} and 142.8 nM for I^-. These values are comparable with or even better than those obtained with other optical analytical methods. Since CPL biosensors are relatively rare to date, our work presents a new horizon for the application of chiral CPL composites in biological assays.

Received 1st August 2024,
Accepted 26th November 2024

DOI: 10.1039/d4nr03178d

rsc.li/nanoscale

1. Introduction

The development of biosensors is promoted by the exploration of innovative methods and devices that can provide efficient, rapid, highly sensitive and selective detection techniques for biomolecules. Among them, optical sensing based on inorganic luminescence materials and technologies offers a multitude of advantages and demonstrates significant capabilities across diverse fields of application.[1] In recent years, there has been a surge of research interest in circularly polarized luminescence (CPL) based on chiral functional luminescent nanomaterials. This novel optical phenomenon has ignited advancements in various fields, including biological imaging, 3D display, optoelectronic recording, and selective photopolymerization.[2] Up to now, researchers have explored a relatively complete path for the preparation of CPL-active materials, and the development of CPL detection technology has attracted much attention. For instance, a novel luminescent probe with chiral adjustability using pyrene derivatives as sensor luminophores was developed, and the detection of Zn^{2+} was achieved using a CPL signal as the output based on its ion dependent assembly characteristics for the first time.[3] Furthermore, our group employed the quenching effect of biological thiol groups on nanocluster CPL and developed a CPL sensor using the right-handed CPL of AuAg nanoclusters as a stable output signal. This sensor was successfully applied for detecting L-Cys.[4] However, so far, the construction of new CPL biosensors and their real-time detection of target analytes still face significant challenges.

Self-assembly supplies a general strategy by placing fluorescent materials in a chiral environment with special environment responses. For instance, achieving CPL can be easily accomplished by covalently bonding or coordinating fluorescent materials with chiral ligands (DNA, helicenes, and metal–organic frameworks).[5] Our group has demonstrated for the first time that human telomeric G-quadruplex (Tel-G4) can serve as an effective DNA template to induce the CPL of non-

[a]*Materials Genome Institute, Shanghai Engineering Research Center of Organ Repair and Shanghai Engineering Research Center for Integrated Circuits and Advanced Display Materials, Shanghai University, Shanghai 200444, China. E-mail: zhenzhen_li@shu.edu.cn, lingyanfeng@t.shu.edu.cn*
[b]*Joint International Research Laboratory of Biomaterials and Biotechnology in Organ Repair, Ministry of Education, Shanghai 200444, China*

† Electronic supplementary information (ESI) available. See DOI: https://doi.org/10.1039/d4nr03178d

chiral fluorescent dyes, and the CPL signal can be regulated by metal ions and temperature, exhibiting stimulus responsive activities.[6] In the development of CPL materials, it is essential to explore new approaches to construct CPL-active materials with a high dissymmetry factor (g_{lum}), which is used to assess the polarization of CPL materials. The g_{lum} value is calculated as $g_{lum} = 2(I_L - I_R)/(I_L + I_R)$, with I_L and I_R representing the intensity of left-handed CPL (L-CPL) and right-handed CPL (R-CPL), respectively.[7,8] The theoretical maximum of $|g_{lum}|$ is 2, indicating complete L-CPL or R-CPL.[9] To date, chiral lanthanide complexes possess significant g_{lum} values due to their large magnetic transition dipole moments, while simple organic molecules typically exhibit strong luminescence but low g_{lum} values (10^{-5}–10^{-3}) due to their large electric dipole transitions.[10–13] Efforts are being made to find CPL-active materials that obtain a balance between the g_{lum} and luminescence efficiency. With the progress of nanomaterials, a range of innovative inorganic luminescent materials like semiconductor quantum dots (QDs), nanoclusters, and carbon dots (CDs) has been created.

As a rising star in the realm of fluorescent nanomaterials, CDs have opened new opportunities in biosensing due to their high photostability, chemical stability, abundant functional groups, good water solubility, excellent biocompatibility, and other advantageous properties.[14,15] The chiral luminescence properties of CDs have been explored for wide applications of chiral CDs with CPL activity in the field of optical sensing. For example, Yang *et al.* described a CPL-active material using nonchiral CDs with different charges assembled with chiral phenylalanine derivatives and obtained spiral supramolecular hydrogels with controllable pitch and diameter, which can be used to effectively distinguish left-handed and right-handed circularly polarized light.[16] The G-quartet-based nanofiber (g-fiber), formed from guanosine 5′-monophosphate (GMP) units linked by hydrogen bonds, serves as an alternative template for self-assembly.[17] Our group has directly constructed the CD composite fluorescent G-quartet hydrogel by a one-step microwave method.[18] It also demonstrates the universality of formation kinetics in regulating the chirality of G-quartet nanofiber structures, providing a high-quality potential chiral environment for the expansion of chiral CD based CPL composites in biosensing functions. However, there are still no reports on expanding the application of such sensitive chiral CD-based CPL composites for biosensing applications, which would pose significant obstacles to their advancement in the field of medical detection. At the same time, this presents vast opportunities for future exploration and study.

Building on the previous extensive investigation of G-quartet nanostructures, we continue to achieve pioneering applications of chiral CD-based CPL composite materials in the realm of biosensing. Herein, we report a novel CPL biosensor for dual detection of Hg^{2+} and I^- using the G-quartet nanofibers and nitrogen sulfur-doped nonchiral CDs (N–S-CDs) for the first time. As shown in Scheme 1, GMP can self-assemble to form a G-quartet structure. A left-handed G-quartet nanofiber and a right-handed G-quartet nanofiber, respectively, were obtained by controlling the rate of product generation. Hence, enantiomeric CPL emission can be obtained by decorating N–S-CDs on these two types of chiral nanofibers creating a strong chiral environment, with a g_{lum} of up to 10^{-2}. In addition, Hg^{2+} has a specific quenching effect on the fluorescence of N–S-CDs, and the addition of I^- can selectively restore the quenched fluorescence intensity. Taking into account the fluorescent switch mechanism on N–S-CDs, the strong CPL emission was initially employed for the precise detection of Hg^{2+} and I^-, with the best results being 83.5 nM (Hg^{2+}) and 142.8 nM (I^-), which sheds light on new directions for the chiral functionalization design of bio-friendly fluorescence sensors.

2. Experimental

2.1. Materials

5′-Guanine monophosphate disodium hydrate (GMP, >99%), strontium nitrate ($Sr(NO_3)_2$), calcium acetate (CA), urea, thiourea, mercury nitrate ($Hg(NO_3)_2$), and sodium iodide (NaI) were all purchased from Shanghai Aladdin Biochemical Technology Co., Ltd. A disposable filter (0.22 μm) was purchased from Millipore, and a dialysis bag (molecular weight cutoff of 1000 Da) was purchased from Shanghai Sangon Biotechnology Co., Ltd. The chemicals used in this project

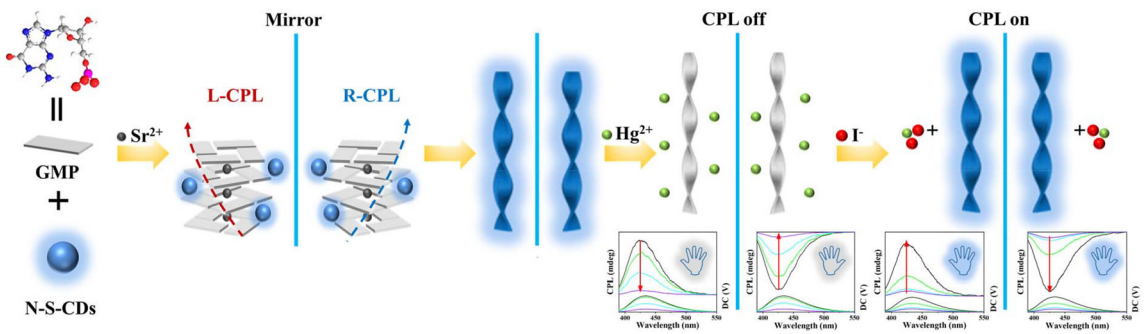

Scheme 1 Schematic illustration of the CPL sensor constructed by the co-assembly of the left-handed and right-handed N–S-CDs/g-fiber.

were used directly without any further processing. All solutions were prepared with ultrapure water (18.2 MΩ cm) from the Milli-Q automatic ultrapure water system.

2.2. Synthesis of N–S-CDs

To synthesize N–S-CDs, we prepared a reaction mixture consisting of 1 g of citric acid (CA), 1 g of urea, and 1 g of thiourea in 10 mL of ultrapure water. The mixture was stirred to ensure homogeneity and then subjected to ultrasonication for 30 minutes to achieve complete dissolution. The resulting solution was transferred to a microwave vial and irradiated in a microwave reactor (CEM Discover SP) at a power setting of 300 W for 5 minutes. The reaction yielded a light-yellow, transparent solution. Insoluble materials were removed by filtration through a disposable filter (0.22 μm), and the filtrate was dialyzed against ultrapure water using a 1000 Da dialysis membrane for 48 hours, with a water change every 12 hours. The purified N–S-CDs solution was then freeze-dried to obtain a solid powder, which was stored at 4 °C for further use.

2.3. Synthesis of the left-handed and right-handed N–S-CDs/g-fiber

First, we prepared GMP solutions at varying concentrations (50, 60, 70, 80, 90, and 100 mM) and added different amounts of N–S-CDs to achieve concentration gradients of 0, 12.5, 25, 37.5, 50, 62.5, and 75 μg mL^{-1}. These solutions were dissolved in 1 mL of ultrapure water and thoroughly mixed. Then, we added $Sr(NO_3)_2$ solutions at different concentrations of 8, 9.6, 11.2, 12.8, 14.4, and 16 mM to each mixture, while maintaining a fixed concentration ratio of GMP to $Sr(NO_3)_2$ at 25 : 4, and gently shook them to ensure complete distribution. After incubating at 15 °C for 4 hours, N–S-CDs self-assembled with GMP to form left-handed and right-handed helical N–S-CDs/g-fibers. Under identical conditions, GMP at different concentrations assembled with N–S-CDs into nanofibers with varying helical chirality.

2.4. Detection of Hg^{2+} and I^-

Using L-/R-CPL of left-handed/right-handed N–S-CDs/g-fiber as the output signal, different concentrations of Hg^{2+} (0, 0.1, 0.5, 1, 3, 5, and 8 μM) were added and allowed to fully react with the assembly at room temperature for 5 minutes. The change in CPL signal intensity at 426 nm wavelength was recorded at an excitation wavelength of 346 nm. Subsequently, under the same testing conditions, different concentrations of lower I^- (0, 0.2, 1, 2, 6, 10, and 16 μM) were added to the left-handed/right-handed Hg^{2+}–N–S-CDs/g-fiber assembly, and the changes in CPL signal intensity were recorded. Under the same conditions, the effects of 8 μM different cations (Al^{3+}, Ba^{2+}, Ca^{2+}, Cd^{2+}, Co^{2+}, Cu^{2+}, Fe^{3+}, Fe^{2+}, K^+, Mg^{2+}, Mn^{2+}, Na^+, Ni^{2+}, Pb^{2+}, and Zn^{2+}) on the CPL of left-handed/right-handed N–S-CDs/g-fiber were tested to evaluate the selectivity of the CPL sensor towards Hg^{2+}. Similarly, the test was conducted to evaluate the selectivity of the sensor towards I^- by testing the effects of different 16 μM reducing substances (Cl^-, Br^-, F^-, CN^-, SCN^-, CH_3COO^-, S^{2-}, GSH, and L-Cys) on the CPL of left-/right-handed Hg^{2+}–N–S-CDs/g-fiber.

3. Results and discussion

3.1. Characterization of N–S-CDs

According to the previous literature, nonchiral N–S-CDs doped with nitrogen and sulfur elements were synthesized using citric acid (CA), urea, and thiourea as raw materials by a one-step microwave method.[19] As shown in Fig. 1a, the size and morphology of N–S-CDs were characterized using TEM, and it was found that they exhibited a spherical like nanoparticle shape and were well dispersed. The particle size statistics in TEM images show that the average size of N–S-CDs is about 2 nm, and high resolution TEM (HRTEM) images of individual N–S-CDs show a clear lattice spacing of 0.21 nm, corresponding to the (100) diffraction surface of graphite carbon, directly proving the typical carbon core structural composition of N–S-CDs.[20]

Preliminary studies were conducted on the structural and optical properties of N–S-CDs using UV-vis and fluorescence (FL) spectroscopy. Fig. 1b illustrates that N–S-CDs exhibit two strong absorption peaks at 200 and 235 nm, with a weaker broad peak near 340 nm. The first two peaks are associated with electronic transitions of C=C, C=N, and C=O from π (or n) to π*,[21] while the latter corresponds to the optimal excitation wavelength of N–S-CDs at 347 nm and leads to the optimal emission wavelength of 442 nm, which can be attributed to the absorption transition of surface functional groups in the 340 nm band.[22] Under UV lamp irradiation, the aqueous solution of N–S-CDs exhibits strong blue fluorescence. In

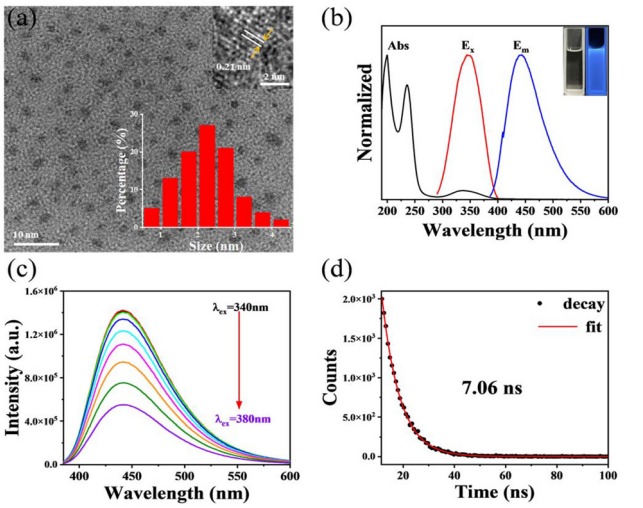

Fig. 1 (a) TEM and HRTEM images of N–S-CDs (inset: histogram of particle size distribution); (b) normalized UV-vis and FL spectra of N–S-CDs (inset: corresponding photos under sunlight (left) and 365 nm ultraviolet light (right)); (c) PL spectra of N–S-CDs at different excitation wavelengths; and (d) time resolved decay spectra and fluorescence lifetime fitting curves of N–S-CDs.

addition, we observed that the N–S-CDs exhibit independent excitation behavior, with their maximum fluorescence emission wavelength remaining unchanged across varying excitation wavelengths (Fig. 1c). This indicates that the N–S-CDs we prepared have a relatively uniform size distribution.[23] Subsequently, we utilized the integrating sphere of the quantum yield measurement system to determine the absolute quantum yield (QY) of N–S-CDs in aqueous solution, which was found to be 24.76% (Fig. S1a†). This value surpasses the 19.2% reported for CDs in the literature, indicating that our synthesis method is more effective in enhancing the quantum yield,[19] which suggests that, under the same conditions, N–S-CDs can more efficiently convert excited energy into fluorescence emission. The time-resolved fluorescence decay spectra of N–S-CDs were also simultaneously analysed to determine their fluorescence lifetime (Fig. 1d). The photoluminescence (PL) decay curve was fitted with a single exponential model, revealing a fluorescence lifetime of approximately 7.06 ns for N–S-CDs, mainly due to surface state photon transitions. Additionally, we conducted an in-depth investigation into its fluorescence stability. After being irradiated using a 150 W xenon lamp for an hour, left standing continuously for 7 days, and exposed to solutions with pH ranging from 4 to 10 and NaCl concentration up to 0.5 M, the fluorescence intensity of N–S-CDs did not show significant changes (Fig. S1b–S1e†). This indicates their enduring resistance to photobleaching and chemical stability under various harsh conditions.

To further reveal the surface properties of N–S-CDs, we first characterized the surface functional groups using FTIR spectroscopy. As shown in Fig. 2a, the absorption bands at 3433 and 3188 cm^{-1} can be attributed to the tensile vibrations of –OH and N–H, respectively.[24] The shoulder peaks near 3050 and 1720 cm^{-1} are characteristic of aromatic C–H stretching vibrations.[25] The absorption peaks at 1666 and 1574 cm^{-1} are attributed to the stretching vibrations of C=O and C–N from the acidic carbon ring, respectively, indicating the formation of –CONR. The peak observed near 1404 cm^{-1} represents the symmetric stretching of C=S,[19] and the surface hydrophilic groups enhance the hydrophilicity and stability of N–S-CDs in aqueous systems. Subsequently, XPS spectroscopy was used to further analyze the surface information of N–S-CDs (Fig. 2b–f), confirming the presence of four main elements: C, N, O, and S. The high-resolution XPS spectrum of C 1s shows three main peaks, with the strongest binding energy peak at 284.8 eV corresponding to the graphite sp^2 carbon structure of N–S-CDs. The peak at 286.75 eV indicates the presence of C–O, C–S, and C–N, while the peak at 288.86 eV can be attributed to the C=O group. In the spectrum of N 1s, peaks corresponding to pyridine nitrogen (399.91 eV) and pyrrole nitrogen (401.71 eV) can be observed. Regarding the O 1s band, the two binding energy peaks at 532.04 and 533.52 eV correspond to C=O and C–O, respectively, while the spectrum of S 2p shows the predominant C–S–C units and a small portion of $–SO_2$ and $–SO_3$ groups in N–S-CDs.[26] The XPS spectral data confirm the analytical conclusion of FTIR and also indicates the successful doping of nitrogen and sulfur elements in N–S-CDs and the formation of various functional groups on the surface.

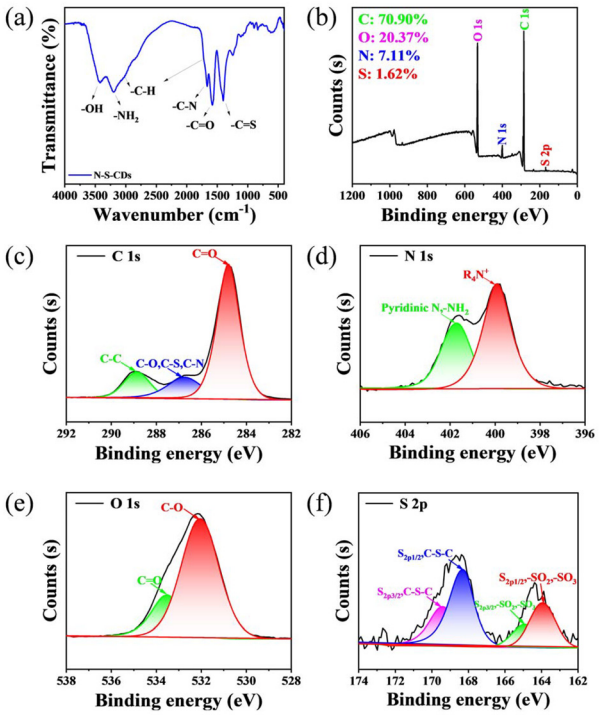

Fig. 2 (a) FTIR spectra of N–S-CDs; (b–f) XPS spectra of N–S-CDs: (b) survey scan; (c) C 1s; (d) N 1s; (e) O 1s; and (f) S 2p.

3.2. Co-assembly and characterization of the left-handed and right-handed N–S-CDs/g-fiber

As a newly developed chiral nanomaterial, helical nanofibers based on G-quartets have been recognized as a highly competitive chiral functional nucleic acid template in the fields of structural chemistry and nanotechnology due to their excellent water solubility and biosafety, and strong chemical compatibility since their debut. They have shown great potential in designing drug carriers, studying dynamic non-covalent interactions, and constructing chiral functionalized biosensors.[27] Metal cations such as K^+, Na^+, Pb^{2+}, and Sr^{2+} are widely recognized for their ability to stabilize G-quartets. These cations interact with four carbonyl oxygen groups, intercalating within the G-quartet structure.[28] In our methodology, Sr^{2+} was specifically selected to induce and stabilize G-quartet nanofibers owing to its exceptional stability when associated with G-quartets.[29] Finally, based on the formation kinetics in the field of molecular self-assembly, the initial reactant concentration was optimised to modify the generation rate and stacking structure of the G-quartet. This adjustment aimed to achieve L-/R-fibers with left and right helical chirality in the nanofibers. Additionally, N–S-CDs were added before the co-assembly. The same combination ratio of GMP and Sr^{2+} was maintained at different reactant concentrations to ensure the desired formation of the G-quartet structure.

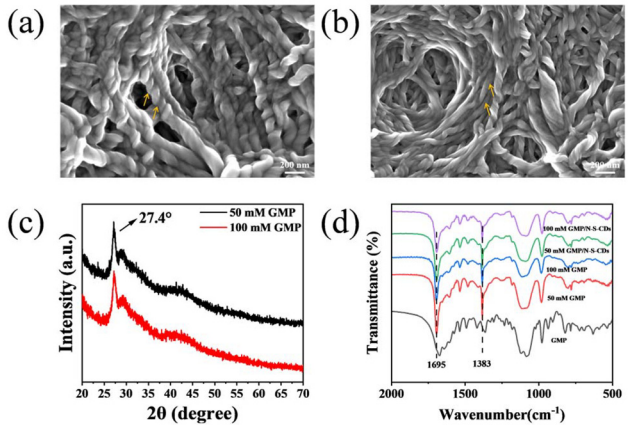

Fig. 3 (a) SEM images of the right-handed N–S-CDs/g-fiber and (b) left-handed N–S-CDs/g-fiber; (c) XRD and (d) FTIR spectra of GMP, right-handed g-fiber, left-handed g-fiber, and N–S-CDs/g-fiber composites.

Fig. 3a presents the SEM image of the right-handed N–S-CDs/g-fiber composite, which was synthesized under the influence of 50 mM GMP and 8 mM Sr^{2+}. The image reveals a nanostructure characterized by a right-handed helical fiber morphology, with fibers having an average width of approximately 150 nm and extending several micrometers in length. These fibers are tightly intertwined, exhibiting a helical spacing of about 50 nm. Importantly, the presence of N–S-CDs does not affect the formation of nanofibers. More interestingly, when we increased the concentrations of GMP and Sr^{2+} to 100 mM and 16 mM, respectively, we obtained left-handed N–S-CDs/g-fiber; the SEM images clearly showed a left-handed helical fiber structure with a similar size and shape to right-handed N–S-CDs/g-fiber (Fig. 3b). To further confirm the basic structural composition of the two composite chiral nanofibers as G-quartet structures, their XRD and FTIR spectra were measured. As shown in Fig. 3c, there is a prominent peak at 27.4° for both left-handed and right-handed N–S-CDs/g-fiber, which may be related to the distance between adjacent vertical G-quartets. This indicates that the stacking characteristic distance between G-quartets is 0.33 nm, providing evidence for the G-quartet nanostructure of the two chiral assembled fibers.[30] The FTIR spectrum (Fig. 3d) reveals the presence of functional groups on the surface of both right-handed and left-handed g-fibers, including amide carbonyl (1695 cm^{-1}), N–H (1524 cm^{-1}), C–N (1482 cm^{-1}), P=O (1086 cm^{-1}), and C–H (1365 cm^{-1}). The absorption peaks at 1695 and 1383 cm^{-1} correspond to the stretching vibration of the C-6=O bond in GMP and the stretching and bending vibrations of the imidazole rings' N-7–C-8 and C-8–H bonds, respectively.[17] These observations confirm the formation of the G-quartet structure through hydrogen bonding between guanine units. Moreover, the similar FTIR spectra of the right-handed and left-handed g-fiber composites indicate that these nanofibers, despite their opposite chiralities, exhibit identical bonding modes. It is worth noting that N–S-CDs may first come into contact with the peripheral phosphate groups of the G-quartet nanofibers, followed by the carbonyl groups, and finally the imidazole rings (Fig. S2†). Consequently, under the influence of metal cations, both chiral g-fiber materials can be easily obtained through self-assembly. They can provide a strong chiral environment for N–S-CDs, resulting in materials that exhibit CPL activity.

In Fig. S3,† we utilized fluorescence microscopy to confirm the assembly of N–S-CDs/g-fiber with both left- and right-handed chiralities. Fig. S3a† depicts the pure R-fiber, which exhibits a flocculent structure in the bright-field image. In the absence of N–S-CDs, these fibers do not emit light in the dark-field image under 405 nm excitation. Fig. S3b and S3c† show bright-field images that reveal the flocculent texture, suggesting that N–S-CDs might be extending the G-quartet nano-helix. The dark-field images captured under 405 nm excitation exhibit these assemblies emitting bright blue fluorescence. These findings confirm the successful assembly of dispersed N–S-CDs into both chiral nanofibers, indicating that the observed fluorescence is not due to the common aggregation-caused quenching (ACQ) effect, which typically leads to fluorescence damping in solution.

The successful assembly of N–S-CDs indicates that the symmetrical helical nanofibers serve as ideal functional nucleic acid chiral templates. They effectively transfer chirality to non-chiral fluorescent N–S-CDs, inducing CPL in the assembly. As shown in Fig. S4,† the R-CPL signal of the right-handed N–S-CDs/g-fiber and the DC value, which symbolizes fluorescence intensity, are continuously enhanced with increasing concentrations of the assembled N–S-CDs. The blue shift of the optimal fluorescence emission peak may be due to the significant influence of chiral templates on the absorption transition of the N–S-CDs' surface states during the assembly process.[31] To explore the assembly limit of chiral fibers on fluorescent substances, optimization experiments were conducted on the assembly concentration of N–S-CDs. When the concentration of N–S-CDs was fixed at 62.5 μg mL^{-1}, the R-CPL intensity and the DC value reached their maximum. Further increases in concentration did not lead to any further changes, indicating that the assembly of N–S-CDs chiral nanofibers has reached saturation. Thus, this concentration is set as the optimal condition for preparing right-handed N–S-CDs/g-fiber. Correspondingly, the L-CPL signal can also be measured through the co-assembly of L-fiber and N–S-CDs, as shown in Fig. S4d.†

Fig. S5a† presents the CD spectra of g-fibers across a range of GMP concentrations from 50 to 100 mM, showing that the CD signal transitions from negative to positive with the increasing concentration of GMP. The symmetric peak at 260 nm and the shoulder at 290 nm are indicative of the formation of the G-quartet,[32] confirming that R-/L-fibers have identical stacking patterns but opposite directions of stacking. Fig. S5b† demonstrates the transition from R-CPL to L-CPL in N–S-CDs/g-fiber nanofibers as the GMP concentration rises from 50 mM to 100 mM. The chirality of the N–S-CDs/g-fiber nanofibers, as verified through CD spectra in the range of

200–800 nm and depicted in Fig. S5c,† aligns with that of the chiral templates of R-/L-fibers shown in Fig. S5a.† This suggests that the chiral helical structure of the g-fibers imparts a strong chirality to the N–S-CD material. Moreover, the maximum g_{lum} values of nonchiral N–S-CDs assembled with L-/R-fibers can reach 0.02 and −0.02, respectively, as shown in Fig. S5d.† This elevated g_{lum} value endows the nanofiber assemblies with significant CPL characteristics, highlighting their potential as highly sensitive CPL sensors.

3.3. CPL detection of Hg^{2+} and I^-

Mercury is a common harmful pollutant in the environment. Its fluidity allows it to diffuse through air and soil, ultimately entering the water system and food chain. Hg^{2+} has been proved to cause damage to human DNA and the central nervous system, and can easily penetrate the skin and respiratory tract.[33] Iodine is an essential trace element and biological anion, which is crucial for human growth and development. A lack of iodine in the diet can lead to several different problems, including thyroid dysfunction, goiter, nerve damage, and paralysis. However, excessive intake of iodine can also lead to thyroid diseases, especially in infants.[34] Therefore, researchers have made many attempts to explore new detection methods for mercury and iodine, which are simple, fast, and highly specific. As shown in Fig. S6a,† the N–S-CDs we synthesized exhibit a fluorescence quenching effect due to the doping of N and S elements after the addition of different concentrations of Hg^{2+} (0–10 μM). The range of Hg^{2+} concentrations has a sensitive fluorescence signal response ability. This may be the result of strong binding between Hg^{2+} and N and S atoms, attributed to their ability to promote electron/hole recombination annihilation through alternating effective electron transfer processes.[35] Furthermore, based on the competitive binding mechanism, we observed that the fluorescence intensity of the N–S-CDs–Hg^{2+} system gradually recovers when I^- is added as the I^- concentration increases from 0 to 20 μM (Fig. S6b†). Meanwhile without the Hg^{2+}, I^- showed no significant effect on the fluorescence intensity of N–S-CDs (Fig. S6c†). According to previous reports, this is due to the strong affinity between Hg^{2+} and I^-, which can form a more stable HgI_2 complex, allowing Hg^{2+} to be completely released from the surface of the N–S-CDs–Hg^{2+} complex, restoring the absorption band and surface functional groups of N–S-CDs to their initial state.[36] The unique fluorescence response of N–S-CDs to Hg^{2+} and I^- also provides an objective basis for potential biosensing applications in the future.

Emerging as a new branch and a promising entity in the realm of fluorescent biosensors, CPL sensors not only offer the advantages of straightforward operation and the sensitive responses typical of optical sensors but also hold significant potential for enantiomeric molecular selective recognition due to their unique chiral emission signals. Despite their potential, CPL output has seen limited application in chiral CD-based fluorescent sensors. We harnessed the fluorescence-responsive properties of N–S-CDs toward Hg^{2+} and I^-, using the chiral environment from L-/R-fiber templates for co-assembly, leading to a novel dual-detecting CPL sensor for Hg^{2+} and I^-. Fig. 4a illustrates the R-CPL strength of right-handed N–S-CDs/g-fiber assemblies decreasing with the Hg^{2+} concentration, correlating with a decrease in the DC value. A strong linear relationship was observed between the logarithm of the CPL inhibition efficiency ($Ln(I_0/I)$) and Hg^{2+} concentrations from 0 to 8 μM, with I_0 and I representing the R-CPL intensities in the absence and presence of Hg^{2+}, respectively (Fig. 4b). At a signal-to-noise ratio of S/N = 3, the limit of detection (LOD) for Hg^{2+} was calculated to be 83.5 nM using LOD = ($3\sigma/S$), where σ is the standard deviation of blank signals and S is the linear curve's slope. Fig. S7a† shows a corresponding decrease in g_{lum} values with increasing Hg^{2+} levels. Subsequently, additional experiments were conducted to explore the secondary detection of I based on the right-handed Hg^{2+}–N–S-CDs/g-fiber (Fig. 4c). It was observed that the value of the R-CPL signal, which had been quenched by Hg^{2+}, gradually recovered with an increased concentration of I^-. The recovery efficiency of CPL inhibited by I^- on the sensor exhibited a linear relationship within the concentration range of 0–16 μM. The LOD for I^- was determined to be 142.8 nM at a signal-to-noise ratio of S/N = 3 (Fig. 4d). Fig. S7b,† showing an increase in g_{lum} values with the addition of I^-, further substantiates the sensor's sensitivity towards changes in the ion concentration.

Similarly, when the L-fiber of the left-handed spiral structure was co-assembled with N–S-CDs, we detected Hg^{2+} and I^- under the same testing conditions using the L-CPL of the assembled body as the output signal. As shown in Fig. 5, the sensor exhibits changes in CPL intensity upon the addition of Hg^{2+} and I^-, showing a linear relationship between the signal value and the concentrations of Hg^{2+} and I^-. The LODs for Hg^{2+} and I^- are found to be 88.4 nM and 157 nM, respectively.

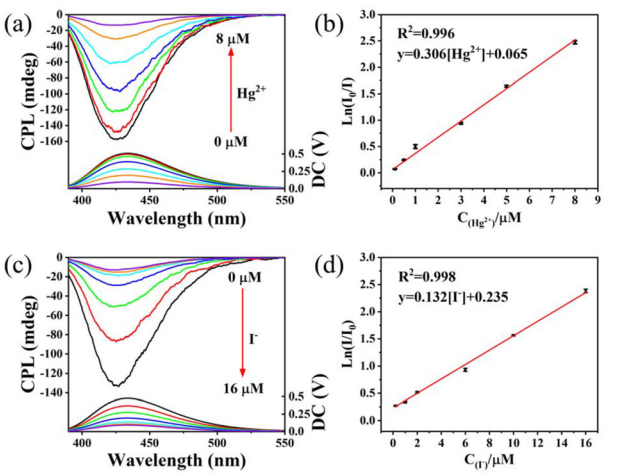

Fig. 4 (a) Representative CPL spectra of the right-handed N–S-CDs/g-fiber with increasing concentrations of Hg^{2+} (0, 0.1, 0.5, 1, 3, 5, and 8 μM); (b) corresponding calibration curve between relative CPL intensity and Hg^{2+} concentration; (c) representative CPL spectra of the right-handed Hg^{2+}–N–S-CDs/g-fiber with increasing concentrations of I^- (0, 0.2, 1, 2, 6, 10, and 16 μM); and (d) corresponding calibration curve between relative CPL intensity and I^- concentration.

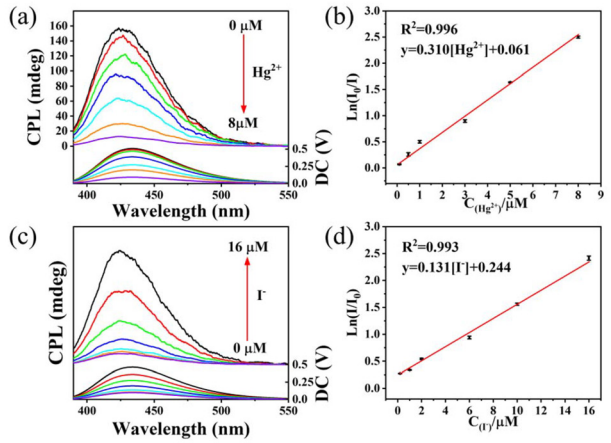

Fig. 5 (a) Representative CPL spectra of the left-handed N–S-CDs/g-fiber with increasing concentrations of Hg^{2+} (0, 0.1, 0.5, 1, 3, 5, and 8 μM); (b) corresponding calibration curve between relative CPL intensity and Hg^{2+} concentration; (c) representative CPL spectra of the left-handed N–S-CD/g-fiber with increasing concentrations of I^- (0, 0.2, 1, 2, 6, 10, and 16 μM); and (d) corresponding calibration curve between relative CPL intensity and I^- concentration.

Moreover, Fig. S8† shows that g_{lum} changes in line with the ion concentrations, which further confirms the sensor's sensitivity to these ions. These values are basically consistent with the data obtained from the left-handed N–S-CDs/g-fiber sensor, confirming the excellent dual sensing function of the CPL sensor fabricated by co-assembling chiral spiral nanofibers with N–S-CDs. The L-/R-composites had similar detection performance.

To further demonstrate the specificity and selectivity of our CPL sensor for detecting Hg^{2+} and I^-, we conducted comparative detection experiments on other metal cations and reducing substances under the same testing conditions. As shown in Fig. 6a, adding 8 μM of Hg^{2+} resulted in a significant decrease of approximately 90% in CPL strength, while the CPL signal of the sensor was not significantly affected by the other metal cations such as Cu^{2+}, Zn^{2+}, Ca^{2+}, and Mg^{2+}. Moreover, adding 16 μM of I^- restored more than 80% of the CPL intensity of the chiral assembly system quenched by Hg^{2+}. In contrast, the recovery effect of other reducing ions and small molecules at the same concentrations on the assembly CPL was almost negligible (Fig. 6b). These results demonstrate that the left-handed and right-handed N–S-CDs/g-fiber composites, as CPL sensors, exhibit excellent selective sensing ability for Hg^{2+} and I^-.

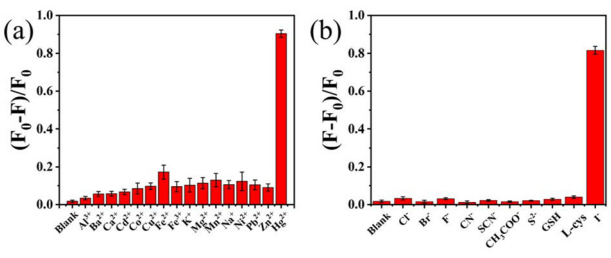

Fig. 6 (a) Selectivity of the CPL sensor for Hg^{2+} and different metal cations; (b) selectivity of the CPL sensor for I^- and different reducing substances.

Furthermore, Tables S1 and S2† summarize a comparison of Hg^{2+} and I^- sensing performance of different detection methods and materials, highlighting the advantages of this proposed CPL detection system in terms of lower LOD and sensitive sensing of the target analytes even in a low concentration range. Therefore, the CPL active material obtained by assembling N–S-CDs with L-/R-fiber as a chiral template shows high specificity and sensitivity for Hg^{2+} and I^- detection. This not only expands the applicability of chiral CD-based CPL composite materials to the field of biosensing but also provides a universal strategy for the design of new biocompatible CPL sensors.

4. Conclusions

In summary, CPL sensors hold significant potential for chiroptical detection. This study commenced with the synthesis of optically stable nonchiral nitrogen N–S-CDs. Subsequently, by meticulously controlling the kinetic formation process of GMP self-assembly and the incorporation of N–S-CDs, we successfully prepared chiral N–S-CDs/g-fiber composites based on the G-quartet structure. These composites, with left- and right-handed helices, served as chiral templates that could transfer chirality to N–S-CDs and induce corresponding CPL signals, characterized by a g_{lum} of 10^{-2}. Furthermore, leveraging the high selectivity and sensitivity of this chiral CD-based CPL composite material, we constructed a detection system for Hg^{2+} and I^- based on CPL sensors for the first time. This approach could, in principle, provide potential chiral discrimination for other targets sensitive to conformational changes. These investigations lay the groundwork for innovative design concepts and application directions in the development of novel CPL-active materials.

Author contributions

Dong Wang: writing – original draft, methodology, investigation, and formal analysis. Zhiwei Zhang: writing – review & editing, methodology and investigation. Xuetao Yan: investigation. Tianliang Li: supervision. Yingying Chen: supervision, funding acquisition, and formal analysis. Zhenzhen Li: writing – review & editing and supervision. Lingyan Feng: writing – review & editing, supervision, project administration, and conceptualization.

Data availability

The data that support the findings of this study are available on request from the corresponding author.

Conflicts of interest

The authors declare no conflict of interest.

Acknowledgements

This work was supported by the Program for Distinguished Professors of Shanghai Universities (Oriental Scholars), Tracking Plan (GZ2022009), the National Natural Science Foundation of China (22177067) and the Shanghai Rising-Star Program (20QA1403400).

References

1 H. Huang, C. He, Y. Zeng, X. Xia, X. Yu, P. Yi and Z. Chen, *Biosens. Bioelectron.*, 2009, **24**, 2255–2259.
2 Y. Yang, R. C. da Costa, M. J. Fuchter and A. J. Campbell, *Nat. Photonics*, 2013, **7**, 634–638.
3 Y. Imai, Y. Nakano, T. Kawai and J. Yuasa, *Angew. Chem., Int. Ed.*, 2018, **57**, 8973–8978.
4 Z. Suo, X. Hou, J. Chen, X. Liu, Y. Liu, F. Xing, Y. Chen and L. Feng, *J. Phys. Chem. C*, 2020, **124**, 21094–21102.
5 Y. Zhang, S. Yu, B. Han, Y. Zhou, X. Zhang, X. Gao and Z. Tang, *Matter*, 2022, **5**, 837–875.
6 J. Chen, Y. Chen, L. Zhao, L. Feng, F. Xing, C. Zhao, L. Hu, J. Ren and X. Qu, *J. Mater. Chem. C*, 2019, **7**, 13947–13952.
7 J. Han, D. Yang, X. Jin, Y. Jiang, M. Liu and P. Duan, *Angew. Chem., Int. Ed.*, 2019, **58**, 7013–7019.
8 T. Zhao, J. Han, X. Jin, Y. Liu, M. Liu and P. Duan, *Angew. Chem., Int. Ed.*, 2019, **58**, 4978–4982.
9 K. Ma, W. Chen, T. Jiao, X. Jin, Y. Sang, D. Yang, J. Zhou, M. Liu and P. Duan, *Chem. Sci.*, 2019, **10**, 6821–6827.
10 J. L. Lunkley, D. Shirotani, K. Yamanari, S. Kaizaki and G. Muller, *J. Am. Chem. Soc.*, 2008, **130**, 13814–13815.
11 M. Sugimoto, X.-L. Liu, S. Tsunega, E. Nakajima, S. Abe, T. Nakashima, T. Kawai and R.-H. Jin, *Chem. – Eur. J.*, 2018, **24**, 6519–6524.
12 H. Tanaka, Y. Inoue and T. Mori, *ChemPhotoChem*, 2018, **2**, 386–402.
13 K. Dhbaibi, L. Favereau, M. Srebro-Hooper, M. Jean, N. Vanthuyne, F. Zinna, B. Jamoussi, L. Di Bari, J. Autschbach and J. Crassous, *Chem. Sci.*, 2018, **9**, 735–742.
14 S. N. Baker and G. A. Baker, *Angew. Chem., Int. Ed.*, 2010, **49**, 6726–6744.
15 H. Li, Z. Kang, Y. Liu and S.-T. Lee, *J. Mater. Chem.*, 2012, **22**, 24230–24253.
16 L. Yang, N. Su, J. Huang, X. Dou, C. Zhao and C. Feng, *Giant*, 2021, **8**, 100077.
17 F. Pu, L. Wu, X. Ran, J. Ren and X. Qu, *Angew. Chem., Int. Ed.*, 2015, **54**, 892–896.
18 Z. Zhang, J. Chen, X. Yan, X. Liu, Y. Chen, C. Zhao and L. Feng, *Carbon*, 2023, **203**, 39–46.
19 R. Tabaraki and N. Sadeghinejad, *Ecotoxicol. Environ. Saf.*, 2018, **153**, 101–106.
20 L. Cai, Z. Fu and F. Cui, *J. Fluoresc.*, 2020, **30**, 11–20.
21 X. Wang, L. Cao, S.-T. Yang, F. Lu, M. J. Meziani, L. Tian, K. W. Sun, M. A. Bloodgood and Y.-P. Sun, *Angew. Chem., Int. Ed.*, 2010, **49**, 5310–5314.
22 S. Lu, L. Sui, J. Liu, S. Zhu, A. Chen, M. Jin and B. Yang, *Adv. Mater.*, 2017, **29**, 1603443.
23 L. Pan, S. Sun, A. Zhang, K. Jiang, L. Zhang, C. Dong, Q. Huang, A. Wu and H. Lin, *Adv. Mater.*, 2015, **27**, 7782–7787.
24 X. Liu, J. Lu, J. Chen, M. Zhang, Y. Chen, F. Xing and L. Feng, *Front. Chem.*, 2020, **8**, 670.
25 Y. Hu, Z. Yang, X. Lu, J. Guo, R. Cheng, L. Zhu, C.-F. Wang and S. Chen, *Nanoscale*, 2020, **12**, 5494–5500.
26 F. Li, Y. Li, X. Yang, X. Han, Y. Jiao, T. Wei, D. Yang, H. Xu and G. Nie, *Angew. Chem., Int. Ed.*, 2018, **57**, 2377–2382.
27 J. T. Davis, *Angew. Chem., Int. Ed.*, 2004, **43**, 668–698.
28 F. M. Chen, *Biochemistry*, 1992, **31**, 3769–3776.
29 B. I. Kankia and L. A. Marky, *J. Am. Chem. Soc.*, 2001, **123**, 10799–10804.
30 A. Ghosh, B. Parasar, T. Bhattacharyya and J. Dash, *Chem. Commun.*, 2016, **52**, 11159–11162.
31 Y. Shi, P. Duan, S. Huo, Y. Li and M. Liu, *Adv. Mater.*, 2018, **30**, 1705011.
32 S. Lena, S. Masiero, S. Pieraccini and G. P. Spada, *Chem. – Eur. J.*, 2009, **15**, 7792–7806.
33 K. Bera, A. K. Das, M. Nag and S. Basak, *Anal. Chem.*, 2014, **86**, 2740–2746.
34 X. Tang, H. Yu, B. Bui, L. Wang, C. Xing, S. Wang, M. Chen, Z. Hu and W. Chen, *Bioact. Mater.*, 2021, **6**, 1541–1554.
35 Q. Xu, Y. Liu, C. Gao, J. Wei, H. Zhou, Y. Chen, C. Dong, T. S. Sreeprasad, N. Li and Z. Xia, *J. Mater. Chem. C*, 2015, **3**, 9885–9893.
36 H. Zhang, Y. Li, X. Liu, P. Liu, Y. Wang, T. An, H. Yang, D. Jing and H. Zhao, *Environ. Sci. Technol. Lett.*, 2014, **1**, 87–91.